applied sciences

MDPI

Article

Facile Synthesis of $NiCo_2S_4$/rGO Composites in a Micro-Impinging Stream Reactor for Energy Storage

Jiawei Zhang, Xiguan Chen, Chunyu Liu and Lixiong Wen *

Research Center of the Ministry of Education for High Gravity Engineering and Technology, Beijing University of Chemical Technology, Beijing 100029, China; 2019400013@buct.edu.cn (J.Z.); 2018200063@buct.edu.cn (X.C.); 2016200079@buct.edu.cn (C.L.)
* Correspondence: wenlx@mail.buct.edu.cn

Abstract: Using a process-enhanced micro-impinging stream reactor (MISR) and a co-precipitation route, $NiCo_2S_4$ and $NiCo_2S_4$/rGO electrode materials were successfully prepared, respectively. Owing to its excellent micromixing performance, the MISR-prepared $NiCo_2S_4$/rGO composites had a smaller size and less agglomeration than the same composites prepared in a traditional stirred reactor (STR). The specific capacity of the MISR-prepared composites was as high as 198.0 mAh g^{-1} under the current density of 1 A g^{-1}. The cycling stability of the composites also improved significantly after being modified with reduced graphene oxide (rGO), and they displayed a fine cycling stability, which maintained a retention rate of 83.6% after 1000 cycles of charging and discharging.

Keywords: micro-impinging stream reactor; micromixing; $NiCo_2S_4$ composite; hybrid supercapacitor

Citation: Zhang, J.; Chen, X.; Liu, C.; Wen, L. Facile Synthesis of $NiCo_2S_4$/rGO Composites in a Micro-Impinging Stream Reactor for Energy Storage. *Appl. Sci.* **2022**, *12*, 2882. https://doi.org/10.3390/app12062882

Academic Editor: Anming Hu

Received: 14 January 2022
Accepted: 8 March 2022
Published: 11 March 2022

1. Introduction

Supercapacitors (SCs) or electrochemical capacitors (ECs) are novel energy storage systems that can complement traditional battery equipment owing to their high power density and excellent cycle stability. Due to different device structures and charging/discharging mechanisms, supercapacitors are divided into three categories: symmetrical supercapacitors, asymmetrical supercapacitors, and hybrid supercapacitors [1]. However, the energy density of supercapacitors cannot be compared with batteries. Therefore, how to solve the defect of low energy density of supercapacitors without reducing power density and cycle life becomes particularly important. Electrical double-layer capacitors (EDLCs) and pseudo-capacitors are the two basic forms of supercapacitors with different energy storage mechanisms [2–4]. With charges accumulating at the electrode/electrolyte interface, the electrical double-layer materials can ensure high power density but low energy density. The specific capacitance and energy density of pseudo-capacitive materials are relatively higher, which depends on the reversible and rapid redox reaction at the surface of electrode materials. Battery-type materials also demonstrate strong Faradaic behavior, which is different with pseudo-capacitive materials [5–7]. Hybrid supercapacitors combine battery-type materials with traditional capacitor materials, which provides a novel form of energy storage and can effectively solve some difficult electrochemical problems [8]. Therefore, researchers have done a lot of work to explore the application of high-performance electrode materials in electrochemical energy storage devices.

Electrochemical energy storage materials include traditional carbon materials, metal compounds, and emerging conductive polymer materials, among which metal oxides and sulfides are widely used [9,10]. In recent years, many reports have indicated that electrochemically active transition metal sulfides (TMSs), especially nickel sulfides (NiS and Ni_2S_3), cobalt sulfides (Co_9S_8 and Co_3S_4), and spinel structure nickel-cobalt sulfides ($NiCo_2S_4$) are effective electrode materials. Compared with their oxide counterparts, they have better conductivity and higher electrochemical activity. In addition, compared with

single-component sulfides, the electrochemical action of nickel-cobalt bimetallic sulfides can give rise to more complex redox reactions, resulting in higher specific capacities [11].

However, $NiCo_2S_4$ is highly dependent on the surface Faraday redox reaction and phase transition process caused by ion intercalation, and the reaction kinetics are unfavorable during the rapid charge and discharge process, leading to poor rate performance and electrochemical stability, which will limit its practical application in hybrid supercapacitor technology [11]. Current studies have found that doping nano-structured electroactive materials on a carbon material substrate may be one of the effective and feasible strategies to solve the above problems [12], which guarantees the efficient utilization of active substances and reaction kinetics. For example, graphene has been reported as an exceptional substrate material for improving the electrochemical activity of ultrafine materials [13,14]. However, due to poor interface bonding with the graphene surface, nanoparticles generally tend to agglomerate and detach from the graphene surface, resulting in a decrease in energy storage performance. Therefore, the application of metal sulfides such as $NiCo_2S_4$ that can bind to the graphene surface stably without agglomerating will be a good solution to improve the performance of its hybrid supercapacitors [15].

$NiCo_2S_4$/rGO composites can be synthesized by different routes, such as hydrothermal [16], electrodeposition [17], co-precipitation [18], and self-template methods [19]. Compared with other methods, co-precipitation has the advantages of a simple preparation process, low cost, and easy control of preparation conditions for large-scale production. The co-precipitation method involves using the precipitant and two or more metal salt solutions to obtain a solid product after co-precipitation. It can precipitate several components at the same time, and the distribution of the components is relatively uniform [20]. It is generally believed that the degree of supersaturation has a great nonlinear effect on the nucleation rate and a high level of supersaturation is the thermodynamic driving force for the phase transition during crystallization processes [21,22]. Since the precipitation process is exceptionally fast, rapid micromixing is essential to create a homogeneous supersaturation, which will in turn ensure the product quality [23]. However, due to the poor micromixing performance and mass transfer efficiency in traditional stirred reactors (STRs), it is difficult to achieve uniform supersaturation, which will have a significant impact on the crystal size distribution and also lead to uneven element distribution in the prepared materials [24].

A proper measure to solve this problem is to develop a reactor with excellent micromixing performance in which a uniform supersaturated environment for nucleation will be provided [25,26]. In the last couple of decades, numerous studies have been invested in the development of microstructure equipment, such as microchannel reactors [27], microfluidic reactors [28], T-mixers [29], and confined impinging jet reactors [30], to enhance the micromixing process. All the reactors mentioned above have the ability to quickly and uniformly mix two miscible fluids, which are suitable for continuous precipitation. However, these devices have various application limitations: (1) the complex structure makes it difficult for manufacturing; (2) some reactors have extremely small inner diameters, which can cause severe blockage problems during precipitation [31,32]. In this regard, the development of new types of micromixing enhancement device, which should be easily constructed and scaled up with slight blockages, is urgently desired for the chemical co-precipitation process.

In this work, we constructed a micro-impinging stream reactor (MISR) based on a capillary reactor and impinging stream technology to enhance the micromixing performance between the reacting fluids for preparing $NiCo_2S_4$/rGO composite materials. The MISR consisted of two stainless steel capillary tubes connected to commercial T-joints with no downstream channel at the outlet, which would greatly reduce the clogging problem and pressure drop in the T-junction chamber. When two fluids converged and collided at the T-shaped intersection, uniform supersaturation could be obtained. The homogeneous environment required for uniform particle co-precipitation was thus guaranteed, which has potential to promote the synergistic effect of hybrid electrode materials, thereby obtaining composite materials with excellent electrochemical properties. In addition, loading of parti-

cles on graphene has also been investigated in MISR to further facilitate the superelectric properties of the $NiCo_2S_4$ composites.

2. Experimental

2.1. Materials

Graphite powder, hydrogen peroxide (H_2O_2, 30% aqueous solution), and hydrazine hydrate ($N_2H_4 \cdot H_2O$, 80% aqueous solution) used to prepare reduced graphene oxide were purchased from Beijing Tongguang Fine Chemical Company. Nickel nitrate hexahydrate ($Ni(NO_3)_2 \cdot 6H_2O$), cobalt nitrate hexahydrate ($Co(NO_3)_2 \cdot 6H_2O$), and sodium sulfide nonahydrate ($Na_2S \cdot 9H_2O$) used to synthesize metal sulfides were provided by Shanghai Macklin Biochemical Technology Co., Ltd. (Shanghai, China). Acetylene black, polyvinylidene fluoride (PVDF), and N-methyl-2-pyrrolidinone (NMP) used for electrode slurry coating were obtained from Shanghai Aladdin Reagent Co., Ltd. (Shanghai, China). Potassium hydroxide (KOH) was supplied by Shanghai Meryer Chemical Technology Co., Ltd. (Shanghai, China). Activated carbon (AC) was purchased from Japan Kuraray Co., Ltd. (Tokyo, Japan). All chemicals involved in this work could be used directly without further treatment.

2.2. Construction of Micro-Impinging Stream Reactor

Figure 1a shows the MISR system, which consists of two parallel stainless steel capillaries and a commercial T-joint (Shanghai Emyte Hydraulic Equipment Co., Ltd., Shanghai, China, SS304), similar to that built in our previous work [33]. The two liquid feeds were introduced from the corresponding capillary tubes and collided in the T-joint cavity with a certain volume flow rate through two advection pumps (China Aerospace Science and Technology Corporation, Beijing Satellite Manufacturing Factory, Beijing, China, 2PB00C) to quickly reach a stable supersaturation state, thereby providing a uniform nucleation environment. Reaction products were collected at the outlet for further processing. Figure 1b is a schematic diagram of the MISR setup. Figure 1c demonstrates the internal structure of the T-joint with geometric details.

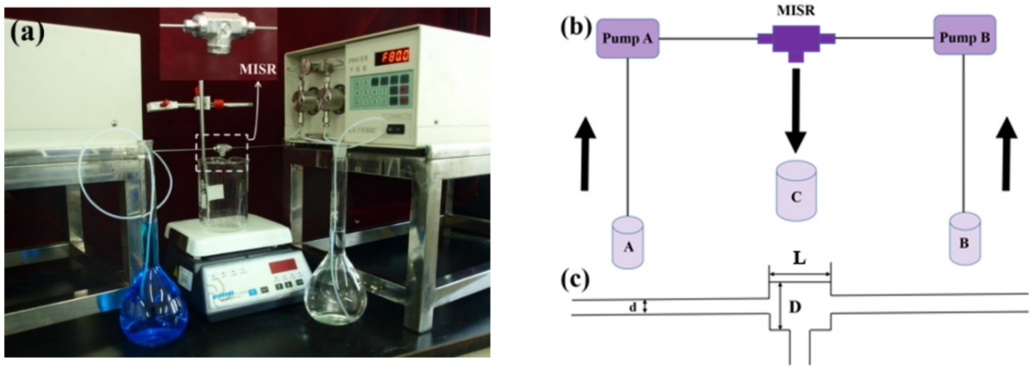

Figure 1. (**a**) MISR experimental system; (**b**) operation flow chart of MISR (A, B, and C are precursor containers and product collector, respectively); (**c**) internal structure of the T-joint (geometric details: inner diameter of the feed pipes d = 0.6 mm, length of the T-joint L = 2 mm, inner diameter of the T-joint D = 1.8 mm).

2.3. Synthesis of NiS, Co_3S_4, and $NiCo_2S_4$

$NiCo_2S_4$ composites were synthesized through a co-precipitation method with MISR as follows: precursor solution A was obtained by slowly dissolving 1.1693 g $Ni(NO_3)_2$ and 0.5915 g $Co(NO_3)_2$ in 100 mL of deionized water. Precursor solution B was prepared by dissolving 1.8133 g $Na_2S \cdot 9H_2O$ in another 100 mL of deionized water. The two precursor solutions were pumped into the MISR through two advection pumps at the same flow rate, and flowed into the collector after impacting in the T-joint. Subsequently, the reaction precipitates in the collector were aged for 3 h. The product was filtered after aging, then

needed to be washed repeatedly with deionized water and absolute ethanol until the pH of the filtrate reached neutral, and was then dried in an oven at 60 °C for 12 h to obtain the final $NiCo_2S_4$ composites. For comparison, the preparation of $NiCo_2S_4$ composites was also carried out under the same conditions in STR. In addition, Co_3S_4 and NiS were prepared in MISR following the same methods as those for $NiCo_2S_4$ composites, but without adding $Ni(NO_3)_2{\cdot}6H_2O$ and $Co(NO_3)_2{\cdot}6H_2O$, respectively.

2.4. Synthesis of $NiCo_2S_4$/rGO Composites

The co-precipitation processes of $NiCo_2S_4$/rGO were carried out in MISR. GO was first prepared with the improved Hummers' method, then reduced to rGO using hydrazine hydrate ($N_2H_4{\cdot}H_2O$) as the reducing agent. In a typical preparation, 0.05 g of GO was dispersed in 100 mL of deionized water and sonicated for 0.5 h. Subsequently, 1.1693 g of $Ni(NO_3)_2{\cdot}6H_2O$ and 0.5915 g of $Co(NO_3)_2{\cdot}6H_2O$ were dissolved in the homogeneous GO dispersion and stirred for 2 h as the precursor solution A. The precursor solution B was obtained by dissolving 1.8133 g $Na_2S{\cdot}9H_2O$ in another 100 mL of deionized water. These two precursor solutions collided at high speed inside the MISR and then flowed into the collector. After aging the precipitates for 3 h, an appropriate amount of $N_2H_4{\cdot}H_2O$ was added to the solution for 1 h reduction treatment at 98 °C. Finally, using the same post-treatment method as the $NiCo_2S_4$ composites, the products were filtered, washed, and dried to obtain the $NiCo_2S_4$/rGO composites.

2.5. Material Characterization

In this work, an Ultima IV X-ray diffractometer (XRD, Rigaku, Tokyo, Japan) was used to test the crystal structure within 5° to 90° at a scan rate of 10° min^{-1}, along with Cu Kα radiation (λ = 1.542 Å). The Raman spectrum was measured and collected by an inVia Reflex confocal Raman microscope (Renishaw, London, UK) with a shift range of 120–3250 cm^{-1}. The three-dimensional morphology and size of the homogeneously dispersed particles were observed through a HITACHI S-4700 field emission scanning electron microscope (SEM, Hitachi, Tokyo, Japan) with an accelerating voltage of 10 kV. The same microscope was used to perform energy dispersive spectroscopy (EDS) analysis at an increased accelerating voltage of 20 kV to determine the element distribution of the particles. A JEOL JEM-3010 transmission electron microscope (TEM, JEOL, Tokyo, Japan) was used to further observe the particle morphology under 120 kV acceleration voltage. The surface chemical compositions were specified by ESCALAB 250 X-ray photoelectron spectroscopy (XPS, THERMO VG, Waltham, MA, USA) with the C 1s peak (284.8 eV) as the standard peak position for charging correction.

2.6. Preparation and Electrochemical Characterization of Electrodes

Powder materials prepared by MISR and traditional STR needed to be further processed for testing. The working electrode of the prepared composites was constructed first. In an agate mortar, the active material, acetylene black (conductive agent), and polyvinylidene fluoride (PVDF binder) were mixed in a mass ratio of 80:15:5, and the mixture was ground until the powder became uniformly black. An appropriate amount of NMP was added dropwise into the powder and stirred well to form a homogeneous slurry. An amount of 3~5 mg of the prepared mixture was pressed on 1 cm^2 of square nickel foam under a pressure of 10 MPa through a tablet press, and then dried at 60 °C in a blast drying oven for 12 h to obtain preliminary electrodes.

The electrochemical performance of the prepared electrodes was characterized with a traditional three-electrode system, in which the electrode to be measured, the Hg/HgO electrode, and the carbon rod were considered as the working electrode, the reference electrode, and the counter electrode, respectively. The aqueous electrolyte was 6 M KOH. Cyclic voltammetry (CV) and galvanostatic charge and discharge (GCD) tests were performed on a CHI660C electrochemical workstation (Shanghai CH Instruments Co., Ltd., China), with voltage windows of 0.5 V and 0.45 V, respectively. Electrochemical impedance

spectroscopy (EIS) was measured at a frequency of 0.01 to 100 kHz under open circuit voltage. The cycle performance was examined by a CT2001A Land Test System (Wuhan Land Electronics Co., Ltd., Wuhan, China). The specific capacity (Q, mAh g^{-1}) was calculated by the following formula:

$$Q = \frac{I\Delta t}{3.6m} \quad (1)$$

where I (A) represents the discharge current, Δt (s) represents the discharge time, and m (g) represents the mass of the active material.

A coin-cell hybrid supercapacitor (HSC) was also assembled using $NiCo_2S_4$/rGO particles, activated carbon (AC), and 6 M KOH as positive electrode, negative electrode, and electrolyte, respectively, and the two electrodes were totally separated with a water-based diaphragm. The electrodes were constructed using the same method. The charge balance between the positive and negative electrodes could be achieved with the mass ratio of the positive and negative active materials according to the following formula:

$$\frac{m_+}{m_-} = \frac{Q_-\Delta V_-}{Q_+\Delta V_+} \quad (2)$$

where m represents the mass of the active material, Q represents the specific capacity, ΔV represents the potential window, and the subscripts "+" and "–" represent the positive and negative electrodes, respectively.

The energy density (E, Wh kg^{-1}) and power density (P, W kg^{-1}) were calculated using the following formulas:

$$E = \frac{C_{cell}V^2}{2 \times 3.6} \quad (3)$$

$$P = \frac{3600E}{\Delta t} \quad (4)$$

where V and Δt represent the potential window (V) and time of discharge (s), respectively, and C_{cell} represents the specific capacitance of the HSC device according to the overall amount of activated materials in both electrodes.

3. Results and Discussion

3.1. Morphological and Electrochemical Characterization of NiS, Co_3S_4, and $NiCo_2S_4$

XRD patterns of NiS, Co_3S_4, and $NiCo_2S_4$ prepared by MISR are shown in Figure 2a. There were four obvious cobalt sulfide diffraction peaks at 2θ = 19.0°, 31.3°, 36.8°, and 51.3° on the Co_3S_4 curve, which corresponded to the plane reflections of (111), (220), (311), and (400) for the spinel Co_3S_4 (JCPDS: 42-1448), respectively. No peaks of other phases appeared in the spectrum, demonstrating that the sample was of high purity. For the NiS curve, the presence of diffraction peaks at 2θ of 19.3°, 34.1°, and 60.3° indicated the successful preparation of NiS (JCPDS: 86-2281). In addition, the XRD curve of $NiCo_2S_4$ composites also showed characteristic peaks of NiS with noticeably lower intensity but shifted to higher positions than those of pure NiS, indicating that Co was doped into the NiS lattice.

Figure 2b presents the cycling performance of the prepared materials to explore the effects of Co doping on the electrochemical performance of NiS at different molar ratios. It shows that Co_3S_4 had the lowest specific capacity (SC) while $NiCo_2S_4$ had the highest SC, but the cycling performance of NiS was the poorest with only 26.2% of its initial capacity retained after 1000 cycles. Therefore, when NiS was doped with Co, not only its specific capacity but also its cycling performance were greatly improved, which can be attributed to the synergistic interaction between Co_3S_4 and NiS in the $NiCo_2S_4$ composites. The optimal mole ratio of Ni^{2+}:Co^{2+} was found to be 2:1 in this work.

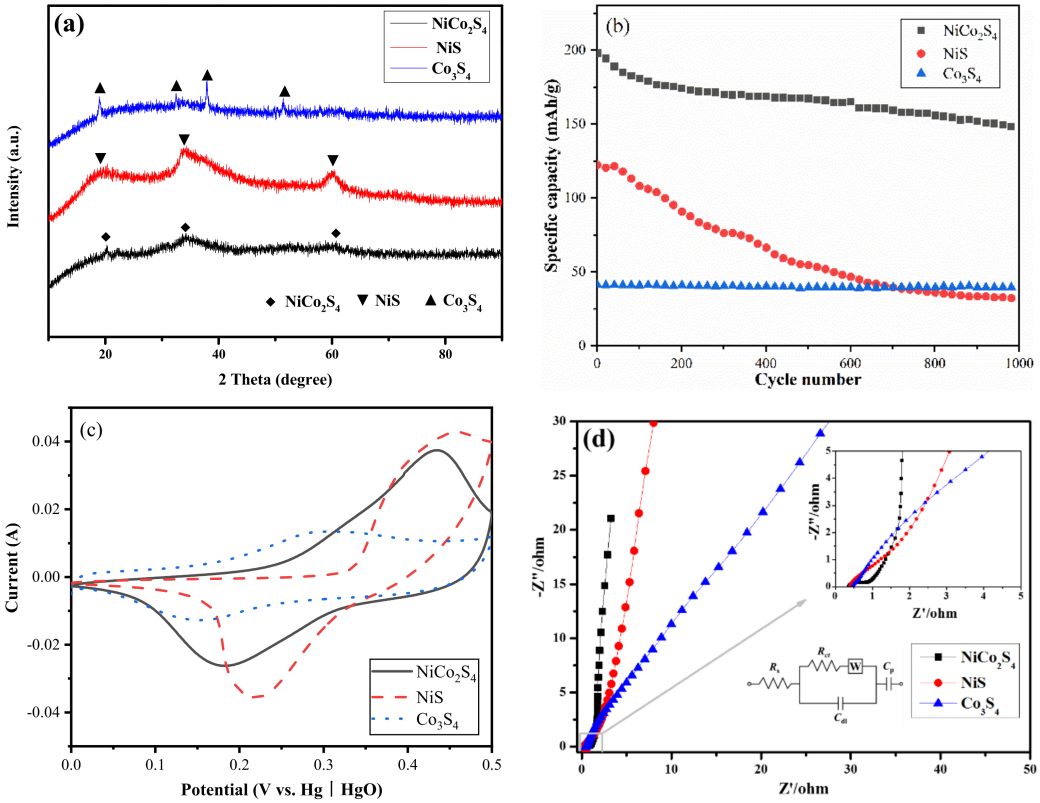

Figure 2. (**a**) XRD analyses; (**b**) cycling stability under a current density of 1 A g^{-1}; (**c**) CV measurements at a scan rate of 5 mV s^{-1}; (**d**) Nyquist spectra (EIS) of the NiS, Co_3S_4, and $NiCo_2S_4$ composites prepared in MISR.

Under the designed voltage window of 0~0.5 V, the electrochemical performance of NiS, Co_3S_4, and $NiCo_2S_4$ as working electrodes was tested at a scan rate of 5 mV s^{-1}. Their obvious difference from the nearly ideal rectangular CV curves of the electric double-layer capacitance was that unique redox peaks were displayed in each of the cyclic voltammetry curves in Figure 2c, indicating the typical Faraday behavior of battery-type electrodes [34]. The redox peak pairs of $NiCo_2S_4$, NiS, and Co_3S_4 electrodes appeared at 0.43/0.18 V, 0.47/0.25 V, and 0.31/0.17 V, respectively, which agreed well with the reversible Faraday reactions between $Co^{2+}/Co^{3+}/Co^{4+}$ and Ni^{2+}/Ni^{3+} combined with OH^- anions, and the charge-discharge mechanism of $NiCo_2S_4$ is listed as follows in Equations (5) and (6) [35]. Obviously, the integrated area enclosed by the CV curve of the $NiCo_2S_4$ composite material was the largest, which indicates that the $NiCo_2S_4$ composite material has the largest specific capacity [36].

$$NiCo_2S_4 + OH^- + H_2O \leftrightarrow NiSOH + 2CoSOH + e^- \quad (5)$$

$$CoSOH + OH^- \leftrightarrow CoSO + H_2O + e^- \quad (6)$$

An EIS test was accomplished in the specified frequency range of 0.01–100 kHz to further explore the electron transfer characteristics of the metal sulfide electrode materials. Figure 2d presents the Nyquist fitting plots of $NiCo_2S_4$, NiS, and Co_3S_4. Due to the Faraday reactions of the electrochemical system, its bulk resistance *R*s could be determined by the value of the intersection of the EIS curve and the *X* axis in the high-frequency region, and the charge transfer resistance *R*ct could be determined by the diameter of the semicircle in the Nyquist diagram [37,38]. The testing results illustrate that the $NiCo_2S_4$ electrode had a relatively lower bulk resistance and smaller charge transfer resistance as compared with the Co_3S_4 and NiS electrodes, demonstrating that the doping of Co into NiS can reduce the intrinsic resistance of the $NiCo_2S_4$ electrode and accelerate the electron transport capability. In the low-frequency region, the slope of the curve was related to the Warburg impedance, which was caused by ion diffusion [39]. The curve slope of the $NiCo_2S_4$ electrode was close

to 90°, which indicates that the ion diffusion in the electrolyte was much faster than that of NiS and Co_3S_4.

To explore the effects of micromixing efficiency of the reactor on the co-precipitation process, $NiCo_2S_4$ composites were prepared using MISR and STR. By SEM observation of the materials in Figure 3a,b, it was found that both composites had an irregular shape. However, the $NiCo_2S_4$ composite prepared by STR was more agglomerated than the sample prepared by MISR, with a larger particle size and uneven distribution. The reason for this phenomenon was that the micromixing performance of MISR was better than that of traditional STR, which was similar to other composite materials prepared by MISR and STR as previously reported [40]. Compared with STR, the porous structure of the composite material obtained by MISR can lead to a larger surface area, which is a great advantage for electrode materials to achieve excellent electrochemical performance. In order to investigate the distribution of the Ni, Co, and S elements in the $NiCo_2S_4$ particles, EDS mapping analysis was performed as illustrated in Figure 3c, showing uniform distribution of all three elements and no other impurity elements observed, which suggests that the products were of high purity.

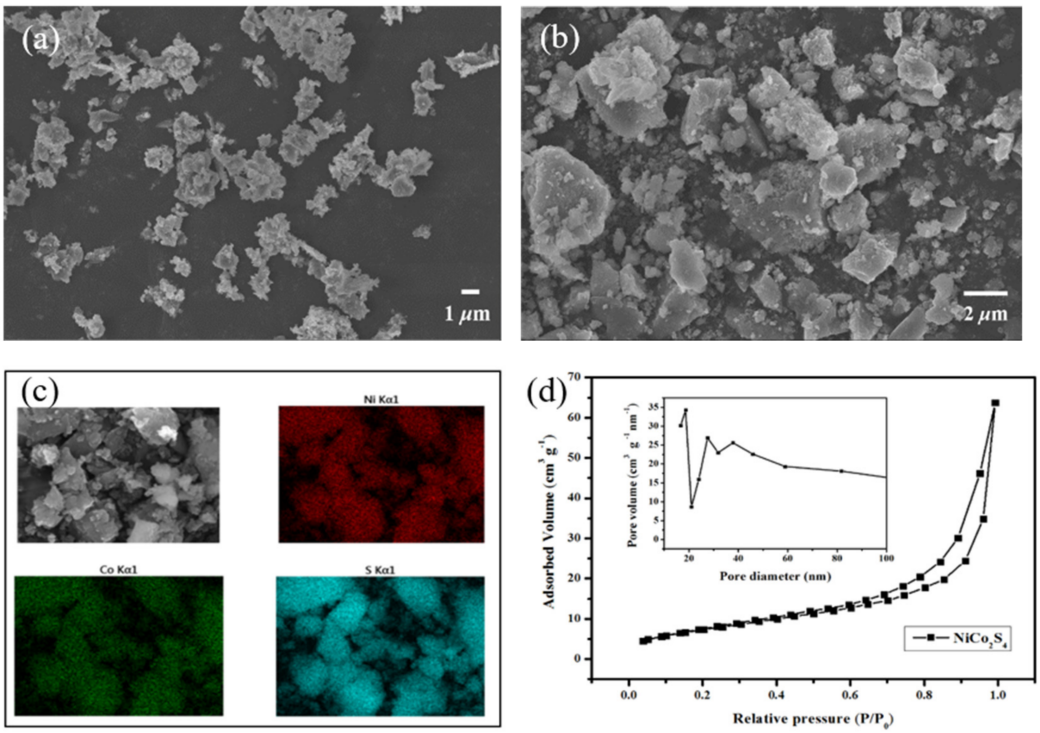

Figure 3. SEM images of (**a**) the MISR-prepared and (**b**) the STR-prepared $NiCo_2S_4$. (**c**) Element distribution (EDS) of the MISR-prepared $NiCo_2S_4$; (**d**) N_2 adsorption/desorption isotherms and PSDs (the insertion) of the MISR-prepared $NiCo_2S_4$.

Porosity and specific surface area are important textural properties that affect the electrochemical performance of materials, and can be obtained by N_2 adsorption and desorption isotherms. The N_2 adsorption and desorption curves of the MISR-prepared $NiCo_2S_4$ shown in Figure 3d displayed typical IV adsorption behavior. The obvious hysteresis loop with relative pressure (P/P_0) in the range 0.6–1.0 indicates that the material had an ordered mesoporous structure. The pore size distribution (PSD) deduced by the separate desorption curve shows that the $NiCo_2S_4$ composite had a wide size distribution between 10 and 100 nm. The sharp peak around 20 nm might be caused by the interspace between $NiCo_2S_4$ particles. The ordered mesoporous structure of $NiCo_2S_4$ resulted in a BET surface area (S_{BET}) of 55.3 m^2 g^{-1}, which was much larger than the S_{BET} values of NiS and Co_3S_4 of 41.5 and 32.7 m^2 g^{-1}, respectively. Previous studies reported that a Faraday redox reaction only occurred on a thin surface of the active electrode materials [40]. Increasing

BET surface area could enhance the effective contact between electrolyte ions and active materials, thereby promoting the electrochemical performance of the prepared $NiCo_2S_4$ composite materials.

The Nyquist plots of the $NiCo_2S_4$ prepared by MISR and STR are presented in Figure 4a. These demonstrate that the *R*s of $NiCo_2S_4$ prepared by MISR was smaller than that prepared by STR, indicating the better diffusion ability of the $NiCo_2S_4$ prepared by MISR. The semicircle in the plot was significantly reduced when changing the reactor from STR to MISR, suggesting the decrease of *R*ct and the enhanced electrical conductivity of the MISR-prepared $NiCo_2S_4$, which could be ascribed to the micromixing intensification in MISR.

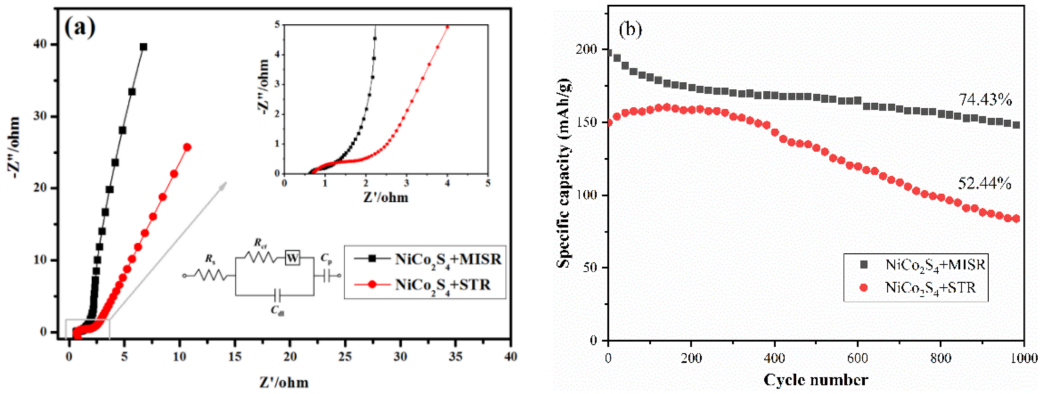

Figure 4. (**a**) EIS Nyquist plots and (**b**) cycling performance of the MISR-prepared and the STR-prepared $NiCo_2S_4$ composites.

The cycling performance of the $NiCo_2S_4$ composites prepared by MISR and STR was investigated as shown in Figure 4b. The results show that the initial specific capacities of the composites prepared by the two methods at a current density of 1 A g^{-1} were 198.0 and 149.9 mAh g^{-1}, and their specific capacities remained 74.43% and 52.44%, respectively, after 1000 cycles of charge-discharge. All results show that the MISR-prepared $NiCo_2S_4$ composite not only had an excellent initial specific capacity, but also had superior cycling performance due to its faster and more uniform ion diffusion.

3.2. Structure and Morphology of rGO

Owing to the large specific surface area and excellent conductivity of reduced graphene oxide (rGO), $NiCo_2S_4$ was also combined with rGO to improve its conductivity and cycling performance.

Graphite was firstly used to synthesize GO by the modified Hummer method and the obtained GO was then reduced with hydrazine hydrate to produce rGO. The rGO Raman curve in Figure 5a shows two high-intensity peaks at 1340 cm^{-1} and 1618 cm^{-1}, which are consistent with the graphene D band and G band (in-plane vibration of sp^2 carbon atoms) [14]. The D and G characteristic peaks of rGO obtained from flake graphite redox were more remarkable than those of GO. The disorder of graphene crystal structure is usually determined by the ratio of D-band and G-band intensity (I_D/I_G), which also represents the defect density of graphene [13]. The value of I_D/I_G in Figure 5a is 1.08, indicating that the rGO prepared by the modified Hummer method was much more disordered than the untreated graphite. In addition, the I_D/I_G value of rGO was also greater than that of the untreated GO, revealing that the average size of the sp^2 domain decreased after GO reduction, which is common in GO and other chemically reduced graphene.

XRD spectra of graphite, GO, and rGO are shown in Figure 5b. All curves display the (002) characteristic diffraction peak of graphene around 25°. Compared with GO, the (001) reflection of rGO almost disappeared, suggesting that GO has been effectively reduced [41].

Figure 5c,d present SEM and TEM images of the prepared rGO. Both images reflect successful synthesis of corrugated rGO. The almost transparent and layered flakes indicate

an ultra-high specific surface area, which could allocate adequate attachment sites for anchoring $NiCo_2S_4$.

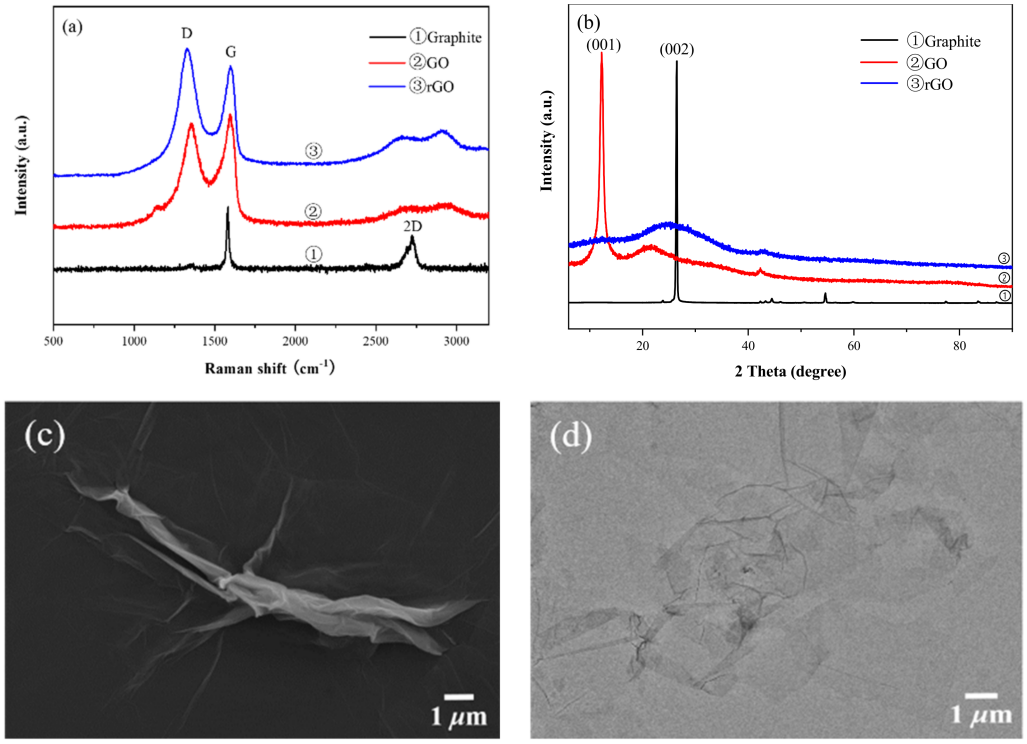

Figure 5. (**a**) Raman spectra and (**b**) XRD spectra of graphite, GO, and rGO; (**c**) SEM and (**d**) TEM image of rGO.

3.3. Electrochemical Properties and Characterization of $NiCo_2S_4$/rGO Composites

As discussed above, the Co doping in MISR has successfully improved the cycling performance of NiS. However, the improvement in conductivity and rate performance of $NiCo_2S_4$ is far from enough. Therefore, the corrugated rGO prepared above was used to modify $NiCo_2S_4$ in MISR. The XRD pattern of the obtained $NiCo_2S_4$/rGO is displayed in Figure 6a. It demonstrates that the rGO modification did not change the original crystal structure of $NiCo_2S_4$. The characteristic peaks of rGO were masked because of its low adding amount, resulting in low diffraction intensity [42]. The above results show that the introduction of rGO would not change the chemical composition of $NiCo_2S_4$.

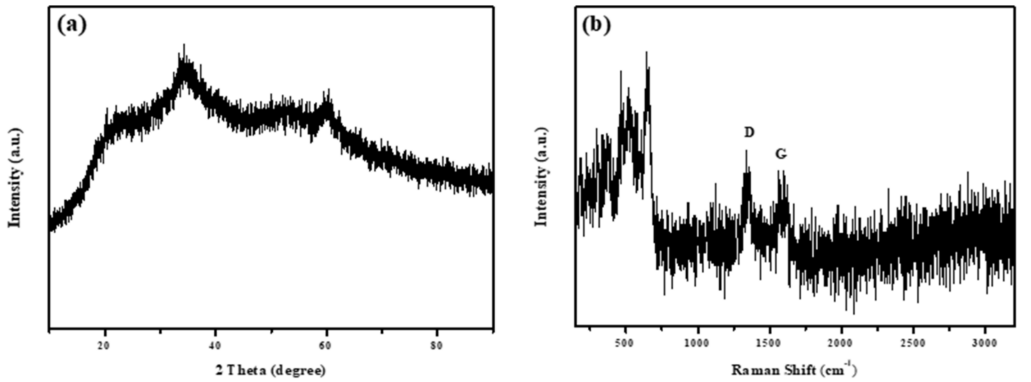

Figure 6. (**a**) XRD pattern and (**b**) Raman spectrum of $NiCo_2S_4$/rGO (D, G: Characteristic peaks of rGO).

Figure 6b displays the Raman spectrum of $NiCo_2S_4$/rGO. Compared with pure rGO, the composites also had two prominent peaks D and G at 1340 and 1618 cm^{-1}, but the intensity was slightly lower. However, the peak-intensity ratio I_D/I_G still maintained a high value of 1.02, which means that the complex reaction did not change the highly disordered structure of rGO, probably because the deposition of $NiCo_2S_4$ particles on the rGO surface could effectively inhibit the stacking of graphene. In addition, there were peaks at 509 cm^{-1} and 661 cm^{-1} belonging to metal sulfides [12], confirming that MISR has successfully loaded $NiCo_2S_4$ onto rGO.

Elemental composition and corresponding chemical states on the surface of the $NiCo_2S_4$/rGO sample were evaluated by XPS. Figure 7a shows an XPS survey spectrum of the $NiCo_2S_4$/rGO sample in the range 100–1100 eV. The peaks at 169.7, 284.1, 781.5, and 855.7 eV correspond to S 2p, C 1s, Co 2p, and Ni 2p, respectively [43], indicating the existence of S, C, Co, and Ni elements in the as-prepared sample. The deconvolution fitting of the Ni 2p high-resolution XPS spectrum (Figure 7b) confirmed the existence of the two spin orbitals of Ni^{2+} and Ni^{3+} corresponding to Ni $2p_{3/2}$ and Ni $2p_{1/2}$. Specifically, the Ni $2p_{3/2}$ spectrum had a peak at 852.8 eV, corresponding to Ni^{2+} ions at the octahedral position, and a peak at 855.9 eV, corresponding to Ni^{3+} ions at the tetrahedral position. The Co 2p XPS spectrum exhibited similar behavior. The convex peaks of Co $2p_{3/2}$ at 778.9 eV and Co $2p_{1/2}$ at 796.3 eV are shown in Figure 8c, indicating that Co^{3+} and Co^{2+} coexisted. The XPS results for nickel and cobalt elements indicate that the prepared $NiCo_2S_4$/rGO hybrids contained Ni (Ni^{2+}, Ni^{3+}) and Co (Co^{2+}, Co^{3+}) with different valence states, which is consistent with the CV analysis. This Faraday behavior guaranteed the excellent electrochemical performance of the as-fabricated electrode materials [44,45]. Figure 7d shows the S 2p spectrum at high resolution, where the two main peaks at approximately 162.5 and 161.5 eV correspond to the metal-sulfur bond and the S^{2-} in low coordination on the surface, respectively. The C 1s XPS curve was fitted by peak splitting and four peaks at 284.6 eV, 285.1 eV, 286.1 eV, and 288.9 eV were obtained, corresponding to the four bonding modes of carbon elements in the $NiCo_2S_4$/rGO composites (carbon-carbon double bond C=C, carbon-oxygen single bond CO, carbonyl carbon C=O, and carboxylic acid carbon OC=O), respectively. This meant that some oxygen-containing functional groups still existed on the graphene surface [42,46], which might help anchor the $NiCo_2S_4$ species on graphene more tightly and strengthen the structure of the hybrid electrodes.

Figure 8 presents TEM and SEM images of the $NiCo_2S_4$/rGO composites. It shows that the composites had a much rougher lamellar structure as compared with the smooth wrinkles of rGO (Figure 5d) due to the anchoring of the bimetallic sulfides on the rGO surface. The $NiCo_2S_4$ anchoring on rGO appeared uniform, which would take full advantage of the excellent conductivity and large specific surface area of rGO. In addition, the tight anchoring of $NiCo_2S_4$ composites on rGO built a barrier-free high-speed transmission channel, which would allow the charge to diffuse quickly and effectively and improve the overall conductivity. From the low-magnification SEM image (Figure 8b), the overall morphology and size distribution of the particles are clearly demonstrated. The particles in the high-magnification SEM image (Figure 8c) exhibited characteristic graphene wrinkles with a grainy surface as a consequence of uniform attachment of $NiCo_2S_4$ nanoparticles. Such attachment could act as a spacer between graphene layers [41], which significantly reduces the agglomeration behavior of rGO. Therefore, $NiCo_2S_4$ and rGO complemented each other and significantly enhanced the superelectric properties of the electrode materials.

Similar three-electrode systems of the $NiCo_2S_4$ composites were built to test the electrochemical properties of $NiCo_2S_4$/rGO, including cyclic voltammetry (CV, Figure 9a), galvanostatic charge and discharge (GCD, Figure 9b), electrochemical impedance (EIS, Figure 9c), and cycling performance (Figure 9d). Using 6 M KOH aqueous solution as the electrolyte, CV curves were obtained at the scan rate range 2 to 40 mV^{-1}. The CV curves were similar to that of the $NiCo_2S_4$ composites, illustrating remarkable Faraday redox peaks caused by the interactions between Co^{2+}/Co^{3+} or Ni^{2+}/Ni^{3+} cations and the OH^- anions from the KOH electrolyte. The CV curve of the material at a scan rate of

5 mV s^{-1} was remarkably symmetrical and the potential difference of the redox peaks was only 209 mV, which was much smaller than that of $NiCo_2S_4$ (259 mV), indicating that the electrochemical reversibility was greatly improved. In addition, as the scan rate increased, a shift in the redox peak could be observed, which was due to the increase in the internal diffusion resistance of the electrode [47].

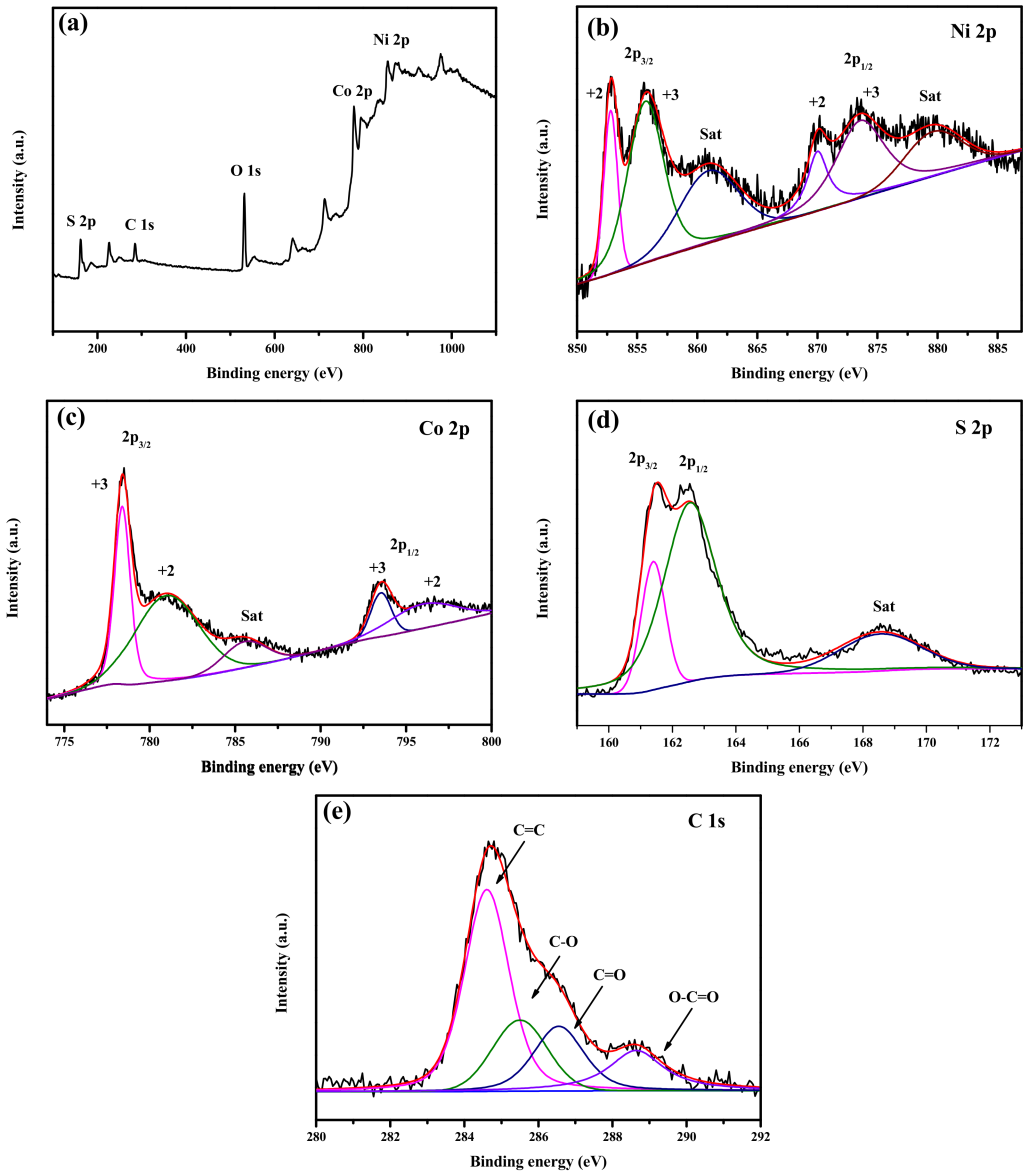

Figure 7. (**a**) XPS spectrum; (**b**) Ni 2p XPS; (**c**) Co 2p XPS; (**d**) S 2p XPS; (**e**) C 1s XPS of $NiCo_2S_4$/rGO composites.

In order to further explore the potential of $NiCo_2S_4$/rGO composites as electrode materials, the constant current charge-discharge performance at different current densities (1 to 20 A g^{-1}) was tested in 6 M KOH electrolyte with the voltage window being set to 0 to 0.5 V (vs. Hg/HgO). Figure 9b illustrates that the initial specific capacity values of the $NiCo_2S_4$/rGO composite were 198.0, 194.1, 188.3, 176.0, 171.4, and 161.1 mAh g^{-1}, respectively, under different current densities of 1, 2, 5, 7, 10, and 20 A g^{-1}. Based on the initial specific capacity at the fixed current density of 1 A g^{-1}, which corresponded to the best performance, the retention rates at another five current densities of 2, 5, 7, 10, and 20 A g^{-1} were 98.0%, 95.1%, 88.8%, 86.5%, and 81.4%, respectively. This shows that an excellent rate performance was achieved by the $NiCo_2S_4$/rGO composite material to

ensure fast charge-discharge ability, due to the special 3D conductive network of the hybrid material for rapid transmission of ions; therefore, it suggests that the rGO sheets are ideal substrates for the uniform nucleation and growth of $NiCo_2S_4$ particles.

Figure 9c reveals the fitting Nyquist plots for the $NiCo_2S_4$ and $NiCo_2S_4$/rGO composites. The semicircle diameter of $NiCo_2S_4$ modified with rGO became smaller, suggesting that the *R*ct was decreased and the electrical conductivity of $NiCo_2S_4$ was enhanced due to the doping of rGO and the even loading process in MISR.

The cycling performance of $NiCo_2S_4$/rGO and $NiCo_2S_4$ composites at a current density of 1 A g^{-1} was recorded as illustrated in Figure 9d. It shows that the initial specific capacities of the two composite materials prepared at the same optimal conditions were 198.0 and 191.8 mAh g^{-1}, respectively. After 1000 charge-discharge cycles, their specific capacity retention rates were 83.6% and 74.4%, respectively. Therefore, the $NiCo_2S_4$ composites modified by rGO had not only higher initial specific capacity, but also more superior cycling performance, because the unique structure of $NiCo_2S_4$/rGO can offer more electroactive sites for rapid diffusion of ions.

Figure 9e,f show the SEM images of NCo_2S_4/rGO before and after the 1000 cycle test. The particles on the electrode sheet consisted of the active material, acetylene black, and the PVDF binder. Their shape and size both remained nearly the same, suggesting that the electrode had good stability during consecutive charge and discharge processes.

Table 1 compares the electrochemical performance of the $NiCo_2S_4$/rGO composites prepared in this study with other similar nickel-cobalt-based sulfide materials by different synthesis methods, all of which have been converted into capacity with the same unit [48]. The electrode materials in this work and the references had the same charge-discharge mechanism with a 3-electron process, implying the same theoretical capacity of 263.8 mAh g^{-1}. This shows that our $NiCo_2S_4$/rGO composite had the highest initial specific capacity, but its cycling stability was not very satisfactory. However, compared with other methods, MISR technology has several significant advantages. Firstly, the MISR equipment is convenient to construct and easy to operate. Then, it can operate continuously to reduce the reaction time dramatically and to assure the stability of product quality. Moreover, the numbering-up technology of MISR can readily increase its production capacity. Hence, the MISR method might be a prospective technology for preparing high-performance composites by co-precipitation.

Figure 8. (**a**) TEM; (**b**) low-magnification and (**c**) high-magnification SEM images of the $NiCo_2S_4$/rGO composites.

In addition, to further explore the electrochemical performance of $NiCo_2S_4$/rGO in specific devices, a simple hybrid supercapacitor (HSC) was constructed as shown in Figure 10a. Figure 10b shows the CV curve of activated carbon as a negative electrode with a voltage window of –1 to 0 V, which maintained the characteristic rectangle of an electric double-layer capacitor. Therefore, the cyclic voltammetry (CV) voltage window of the HSC device shown in Figure 10b should be set to 1.5 V. CV curves of the ASC device at various scan rates (10 to 100 mV s^{-1}) are presented in Figure 10c. The broad redox peak indicates that the HSC device composed of $NiCo_2S_4$/rGO had the battery-type capacity. The charging and discharging platform of the HSC device is not obvious in Figure 10d, but

it shows an almost axisymmetric curve, suggesting an excellent capacitive characteristic. At different current densities of 1, 2, 5, 7, and 10 A g^{-1}, the initial specific capacitances of the HSC device were obtained as 121.2, 107.8, 92.0, 86.6, and 77.5 F g^{-1}, respectively. Moreover, the HSC device demonstrated a fine cycling performance, with a capacitance retention rate of 83.8% after 1000 cycles at a current density of 1 A g^{-1} (Figure 10e). The coulombic efficiency of this hybrid device is also shown in Figure 10e, which has remained above 98.6% during the entire cycle test process. Figure 10f shows the corresponding IR drop of the device at different current densities. It had the smallest IR drop of 0.092 V at a current density of 1 A g^{-1}, and the IR drops at 2, 5, and 7A g^{-1} were 0.119 V, 0.126 V, and 0.180 V, respectively, demonstrating a small increase of the IR drop within such a current density range. When the current density reached 10 A g^{-1}, the IR drop increased to 0.658 V sharply. Therefore, the HSC device had a good electrochemical performance at low current densities.

Table 1. Electrochemical comparison of NiCo-based sulfides synthesized by different methods.

Materials	Methods	Capacity	Capacity Retention Rate
$NiCo_2S_4$/rGO (This work)	MISR	198 mAh g^{-1} (1 A g^{-1})	83.6% (1 A g^{-1}, 1000 cycles)
Tube-like $NiCo_2S_4$ [49]	Solvothermal method	116.4 mAh g^{-1} (3 A g^{-1})	75.9% (10 A g^{-1}, 5000 cycles)
$Ni_{1.5}Co_{1.5}S_4$ [12]	Polyol method	167.0 mAh g^{-1} (1 A g^{-1})	108% (10 A g^{-1}, 2000 cycles)
$NiCo_2S_4$ arrays on nickel foam [50]	Hydrothermal method	102.2 mAh g^{-1} (0.5 A g^{-1})	85% (5 A g^{-1}, 5000 cycles)

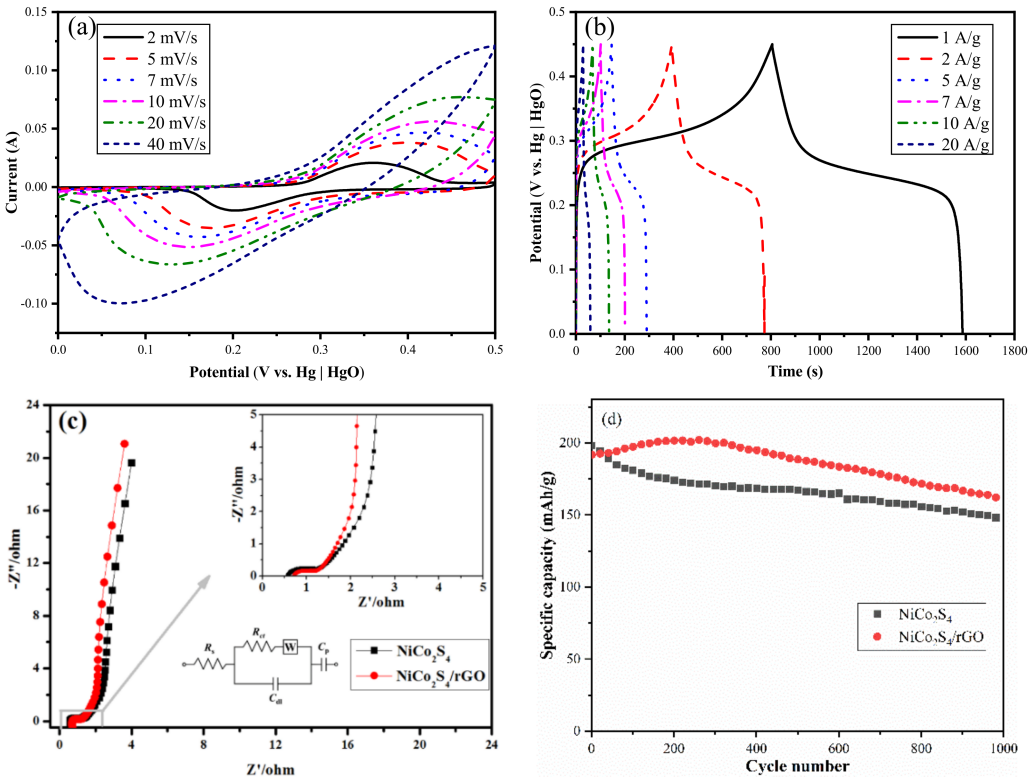

Figure 9. *Cont.*

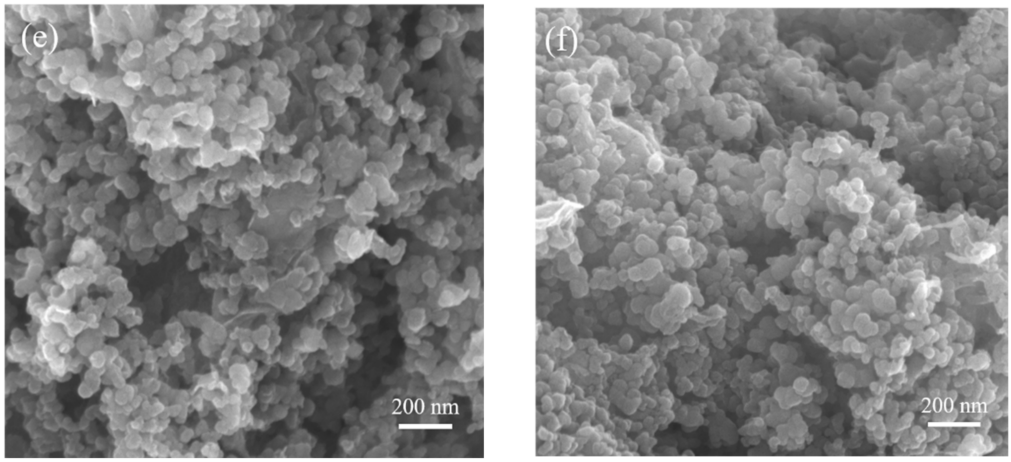

Figure 9. (**a**) CV curves at various scan rates, (**b**) galvanostatic charge and discharge diagram at different current densities, (**c**) EIS spectra, and (**d**) cycling performance of the $NiCo_2S_4$/rGO composites; SEM images of $NiCo_2S_4$/rGO composites (**e**) before and (**f**) after 1000 charge-discharge cycles.

There are two other important electrochemical properties of electrode materials that have often been ignored by researchers, i.e., the self-discharge and leakage current of hybrid devices. In this work, the device was firstly charged to 1.5 V under a very small current density, and then kept at this voltage for 1 h. The current change over such time was recorded to obtain the leakage current curve, as shown in Figure 11a. It can be observed that the leakage current dropped rapidly from the initial 1.9 mA to 0.33 mA within the first 10 min. After that, the leakage current decreased slowly and was finally stabilized at 0.25 mA. For water-based hybrid supercapacitors studied in the past, a leakage current of 0.0255 mA per mg was regarded as an extremely low value, indicating that our device had excellent cycle stability. In addition, in order to further evaluate the charge retention performance of the hybrid device, a self-discharge test was performed by charging the device to 1.5 V with the same method used in the leakage current test, and then removing the power supply and letting it stand for 30 min, as shown in Figure 11b. Unlike the leakage current, self-discharge maintained a mild trend throughout the test. The initial voltage was 1.460 V and remained at 1.216 V after 1 h with a potential difference of 0.244 V, which indicates that this device has an excellent self-discharge performance and hence will have an appealing prospect in the field of energy storage.

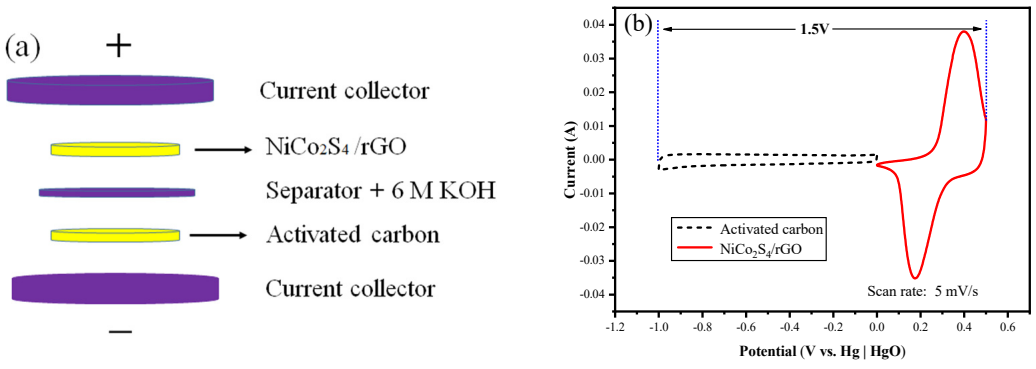

Figure 10. *Cont.*

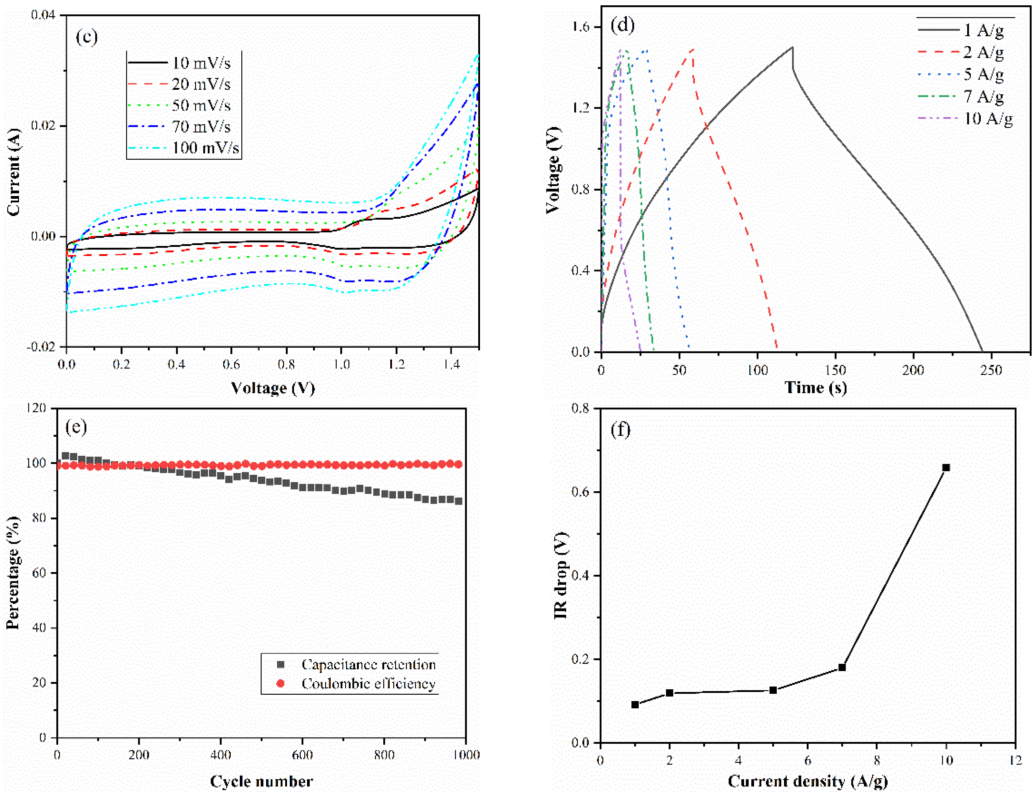

Figure 10. (**a**) Scheme of the hybrid supercapacitor ($NiCo_2S_4$/rGO//activated carbon); (**b**) CV measurements of $NiCo_2S_4$/rGO and activated carbon electrodes at a scan rate of 5 mV s^{-1} in a three-electrode system; (**c**) CV curves of $NiCo_2S_4$/rGO//activated carbon HSC device at different scan rates; (**d**) initial GCD curves of $NiCo_2S_4$/rGO//activated carbon HSC device at different current densities; (**e**) the cycle stability and coulombic efficiency of $NiCo_2S_4$/rGO//activated carbon HSC device at a current density of 1 A g^{-1}; (**f**) IR drop of HSC device under different current densities.

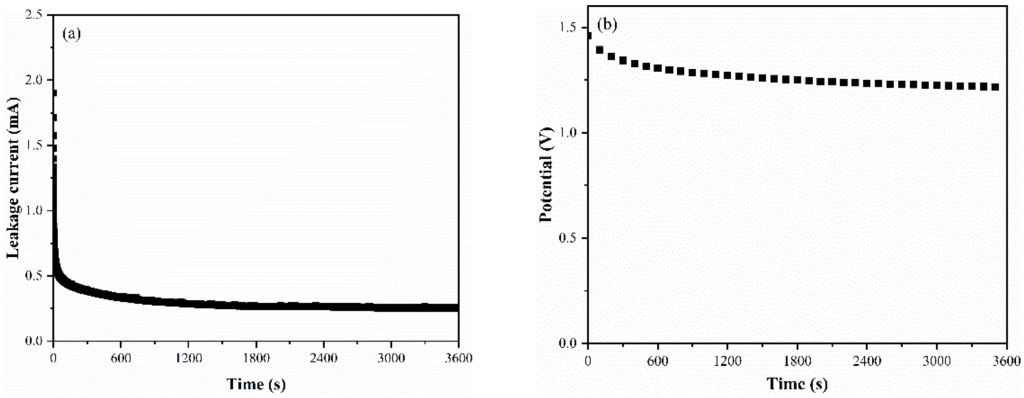

Figure 11. (**a**) Leakage current and (**b**) self-discharge of supercapacitor device.

4. Conclusions

This work constructed a new type of micro-impinging stream reactor (MISR), and explored the syntheses of NiS, Co_3S_4, $NiCo_2S_4$, and $NiCo_2S_4$/rGO composites by the co-precipitation process using this equipment and their applications in hybrid supercapacitor electrode materials. As compared to NiS and Co_3S_4, the $NiCo_2S_4$ composites were found to possess several advantages such as smaller particle size, more uniform mesoporous structure, larger specific surface area and, in turn, more superior electrochemical performance. In addition, $NiCo_2S_4$ could be quickly anchored on the surface of rGO through MISR to enhance its performance. The $NiCo_2S_4$/rGO composites had the highest specific capacity

of 198.0 F g^{-1} and the capacity retention after 1000 electrochemical cycles was 83.6% under a current density of 1 A g^{-1}. Changing the current density to 20 A g^{-1}, the specific capacity of $NiCo_2S_4$/rGO could reach 161.1 mAh g^{-1}, and the retention rate was 81.4%, suggesting an outstanding rate capability. Furthermore, the $NiCo_2S_4$/rGO//AC asymmetric supercapacitor exhibited a fine cycling performance with 83.8% of the maximum capacitance retention after 1000 electrochemical cycles at a current density of 1 A g^{-1}. This work shows that the MISR method may have great prospects in preparing high-performance ultrafine composites.

Author Contributions: Conceptualization, J.Z. and L.W.; methodology, J.Z. and L.W.; investigation, J.Z., X.C. and C.L.; resources, L.W. and X.C.; data curation, J.Z.; writing—original draft preparation, J.Z. and X.C.; writing—review and editing, J.Z. and L.W.; supervision, L.W.; funding acquisition, L.W. All authors have read and agreed to the published version of the manuscript.

Funding: This research was funded by the Major Project of National Science and Technology from China (No. 2018ZX09721002-002), the National Key R&D Program of China (No. 2017YFB0307202), and the National Natural Science Foundation of China (Nos. 21576012).

Institutional Review Board Statement: Not applicable.

Informed Consent Statement: Not applicable.

Conflicts of Interest: The authors declare no conflict of interest.

References

1. Wang, T.; Chen, H.; Yu, F.; Zhao, X.; Wang, H. Boosting the Cycling Stability of Transition Metal Compounds-based Supercapacitors. *Energy Storage Mater.* **2019**, *16*, 545–573. [CrossRef]
2. Forse, A.C.; Merlet, C.; Griffin, J.M.; Grey, C.P. New Perspectives on the Charging Mechanisms of Supercapacitors. *J. Am. Chem. Soc.* **2016**, *138*, 5731–5744. [CrossRef] [PubMed]
3. Lokhande, P.E.; Chavan, U.S.; Pandey, A. Materials and Fabrication Methods for Electrochemical Supercapacitors: Overview. *Electrochem. Energy Rev.* **2020**, *3*, 155–186. [CrossRef]
4. Sharma, P.; Kumar, V. Current Technology of Supercapacitors: A Review. *J. Electron. Mater.* **2020**, *49*, 3520–3532. [CrossRef]
5. Oliva, P.; Leonardi, J.; Laurent, J.F.; Delmas, C.; Braconnier, J.J.; Figlarz, M. Review of the Structure and the Electrochemistry of Nickel Hydroxides and Oxy-hydroxides. *J. Power Sources* **1982**, *8*, 229–255. [CrossRef]
6. Brousse, T.; Bélanger, D.; Long, J.W. To be or Not to be Pseudocapacitive. *J. Electrochem. Soc.* **2015**, *162*, A5185–A5189. [CrossRef]
7. Bélanger, D.; Brousse, T.; Sugimoto, W.; Long, J.W.; Balducci, A. A Guideline for Reporting Performance Metrics with Electrochemical Capacitors: From Electrode Materials to Full Devices. *J. Electrochem. Soc.* **2017**, *164*, A1487–A1488.
8. Pell, W.G.; Conway, B.E. Peculiarities and Requirements of Asymmetric Capacitor Devices Based on Combination of Capacitor and Battery-type Electrodes. *J. Power Sources* **2004**, *136*, 334–345. [CrossRef]
9. Ansari, S.A.; Parveen, N.; Al-Othoum, M.A.S.; Ansari, M.O. Effect of Washing on the Electrochemical Performance of a Three-dimensional Current Collector for Energy Storage Applications. *Nanomaterials* **2021**, *11*, 1596. [CrossRef]
10. Parveen, N.; Ansari, S.A.; Ansari, M.Z.; Ansari, M.O. Manganese Oxide as an Efective Electrode Material for Energy Storage: A Review. *Environ. Chem. Lett.* **2021**, *21*, 01316.
11. Lu, F.; Zhou, M.; Li, W.; Weng, Q.; Li, C.; Xue, Y.; Jiang, X.; Zeng, X.; Bando, Y.; Golberg, D. Engineering Sulfur Vacancies and Impurities in $NiCo_2S_4$ Nanostructures Toward Optimal Supercapacitive Performance. *Nano Energy* **2016**, *26*, 313–323. [CrossRef]
12. Chen, H.; Jiang, J.; Zhao, Y.; Zhang, L.; Guo, D.; Xia, D. One-pot Synthesis of Porous Nickel Cobalt Sulphides: Tuning the Composition for Superior Pseudocapacitance. *J. Mater. Chem. A* **2015**, *3*, 428. [CrossRef]
13. Peng, S.; Li, L.; Li, C.; Tan, H.; Cai, R.; Yu, H.; Mhaisalkar, S.; Srinivasan, M.; Ramakrishna, S.; Yan, Q. In Situ Growth of $NiCo_2S_4$ Nanosheets on Graphene for High-performance Supercapacitors. *Chem. Commun.* **2013**, *49*, 10178–10180. [CrossRef]
14. Yang, J.; Yu, C.; Fan, X.; Liang, S.; Li, S.; Huang, H.; Ling, Z.; Hao, C.; Qiu, J. Electroactive Edge Site-enriched Nickel–cobalt Sulfide into Graphene Frameworks for High-performance Asymmetric Supercapacitors. *Energy Environ. Sci.* **2016**, *9*, 1299–1307. [CrossRef]
15. Yan, J.; Fan, Z.; Sun, W.; Ning, G.; Wei, T.; Zhang, Q.; Zhang, R.; Zhi, L.; Wei, F. Advanced Asymmetric Supercapacitors Based on $Ni(OH)_2$/Graphene and Porous Graphene Electrodes with High Energy Density. *Adv. Funct. Mater.* **2012**, *22*, 2632–2641. [CrossRef]
16. Li, Z.; Li, X.; Xiang, L.; Xie, X.; Li, X.; Xiao, D.; Shen, J.; Lu, W.; Lu, L.; Liu, S. Three-dimensional Hierarchical Nickel–cobalt–sulfide Nanostructures for High Performance Electrochemical Energy Storage Electrodes. *J. Mater. Chem. A* **2016**, *4*, 18335–18341. [CrossRef]
17. Shen, L.; Wang, J.; Xu, G.; Li, H.; Dou, H.; Zhang, X. $NiCo_2S_4$ Nanosheets Grown on Nitrogen-Doped Carbon Foams as an Advanced Electrode for Supercapacitors. *Adv. Energy Mater.* **2015**, *5*, 1400977. [CrossRef]

18. Hong, W.; Wang, J.; Li, Z.; Yang, S. Fabrication of Co_3O_4@Co–Ni Sulfides Core/shell Nanowire Arrays as Binder-free Electrode for Electrochemical Energy Storage. *Energy* **2015**, *93*, 435–441. [CrossRef]
19. Shen, L.; Yu, L.; Wu, H.; Yu, X.; Zhang, X.; Lou, X. Formation of Nickel Cobalt Sulfide Ball-in-ball Hollow Spheres with Enhanced Electrochemical Pseudocapacitive Properties. *Nat. Commun.* **2015**, *6*, 6694. [CrossRef]
20. Jiao, Z.; Luan, J.; Miller, M.K.; Chung, Y.W.; Liu, C. Co-precipitation of Nanoscale Particles in Steels with Ultra-high Strength for a New Era. *Mater. Today* **2017**, *20*, 142–154. [CrossRef]
21. Cocero, M.J.; Martín, Á.; Mattea, F.; Varona, S. Encapsulation and Co-precipitation Processes with Supercritical Fluids: Fundamentals and Applications. *J. Supercrit. Fluids* **2009**, *47*, 546–555. [CrossRef]
22. Carolin, C.F.; Kumar, P.S.; Saravanan, A.; Joshiba, G.J.; Naushad, M. Efficient Techniques for the Removal of Toxic Heavy Metals from Aquatic Environment: A Review. *J. Environ. Chem. Eng.* **2017**, *5*, 2782–2799. [CrossRef]
23. Hernández-Uresti, D.B.; Martínez-de la Cruz, A.; Torres-Martínez, L.M. Photocatalytic Properties of $PbMoO_4$ Synthesized by Co-precipitation Method: Organic Dyes Degradation under UV irradiation. *Res. Chem. Intermed.* **2011**, *38*, 817–828. [CrossRef]
24. Huber, F.; Venvik, H.; Ronning, M.; Walmsley, J.; Holmen, A. Preparation and Characterization of Nanocrystalline, High-surface Area CuCeZr Mixed Oxide Catalysts from Homogeneous Co-precipitation. *Chem. Eng. J.* **2008**, *137*, 686–702. [CrossRef]
25. Wiles, C.; Watts, P. Continuous Flow Reactors: A Perspective. *Green Chem.* **2012**, *14*, 38–54. [CrossRef]
26. DeMello, A.J. Control and Detection of Chemical Reactions in Microfluidic Systems. *Nature* **2006**, *442*, 394–402. [CrossRef]
27. Theberge, A.B.; Courtois, F.; Schaerli, Y.; Fischlechner, M.; Abell, C.; Hollfelder, F.; Huck, W.T. Microdroplets in Microfluidics: An Evolving Platform for Discoveries in Chemistry and Biology. *Angew. Chem. Int. Ed. Engl.* **2010**, *49*, 5846–5868. [CrossRef]
28. Khan, S.A.; Gunther, A.; Schmidt, M.A.; Jensen, K.F. Microfluidic Synthesis of Colloidal Silica. *Langmuir* **2004**, *20*, 8604–8611. [CrossRef]
29. Roberge, D.M.; Ducry, L.; Bieler, N.; Cretton, P.; Zimmermann, B. Microreactor Technology: A Revolution for the Fine Chemical and Pharmaceutical Industries? *Chem. Eng. Technol.* **2005**, *28*, 318–323. [CrossRef]
30. Geyer, K.; Codee, J.D.; Seeberger, P.H. Microreactors as Tools for Synthetic Chemists—The Chemists' Round-bottomed Flask of the 21st Century? *Chemistry* **2006**, *12*, 8434–8442. [CrossRef]
31. Kiwi-Minsker, L.; Renken, A. Microstructured Reactors for Catalytic Reactions. *Catal. Today* **2005**, *110*, 2–14. [CrossRef]
32. Watts, P.; Haswell, S.J. The Application of Micro Reactors for Organic Synthesis. *Chem. Soc. Rev.* **2005**, *34*, 235–246. [CrossRef] [PubMed]
33. Zhang, Q.; Tian, L.; Wu, Y.; Li, Y.; Wen, L.; Wang, S. Fast Coprecipitation of Nickel-cobalt Oxide in a Micro-impinging Stream Reactor for the Construction of High-performance Asymmetric Supercapacitors. *J. Alloys Compd.* **2019**, *792*, 314–327. [CrossRef]
34. Cheng, M.; Fan, H.; Song, Y.; Cui, Y.; Wang, R. Interconnected Hierarchical $NiCo_2O_4$ Microspheres as High-performance Electrode Materials for Supercapacitors. *Dalton Trans.* **2017**, *46*, 9201–9209. [CrossRef]
35. Xie, J.; Yang, Y.; Li, G.; Xia, H.; Wang, P.; Sun, P.; Li, X.; Cai, H.; Xiong, J. One-step Sulfuration Synthesis of Hierarchical $NiCo_2S_4$@$NiCo_2S_4$ Nanotube/nanosheet Arrays on Carbon Cloth as Advanced Electrodes for High-performance Flexible Solid-state Hybrid Supercapacitors. *RSC. Adv.* **2019**, *9*, 3041–3049. [CrossRef]
36. Xiong, S.; Chen, J.; Lou, X.; Zeng, H. Mesoporous Co_3O_4 and CoO@C Topotactically Transformed from Chrysanthemum-like $Co(CO_3)_{0.5}(OH)_{0.11}H_2O$ and Their Lithium-Storage Properties. *Adv. Funct. Mater.* **2012**, *22*, 861–871. [CrossRef]
37. Huang, Y.; Shi, T.; Jiang, S.; Cheng, S.; Tao, X.; Zhong, Y.; Liao, G.; Tang, Z. Enhanced Cycling Stability of $NiCo_2S_4$@NiO Core-shell Nanowire Arrays for All-solid-state Asymmetric Supercapacitors. *Sci. Rep.* **2016**, *6*, 38620. [CrossRef]
38. Xiao, J.; Wan, L.; Yang, S.; Xiao, F.; Wang, S. Design Hierarchical Electrodes with Highly Conductive $NiCo_2S_4$ Nanotube Arrays Grown on Carbon Fiber Paper for High-performance Pseudocapacitors. *Nano Lett.* **2014**, *14*, 831–838. [CrossRef]
39. Mei, L.; Yang, T.; Xu, C.; Zhang, M.; Chen, L.; Li, Q.; Wang, T. Hierarchical Mushroom-like $CoNi_2S_4$ Arrays as a Novel Electrode Material for Supercapacitors. *Nano Energy* **2014**, *3*, 36–45. [CrossRef]
40. Ma, M.; Zhang, C.; Huang, G.; Xing, B.; Zhang, C. Synthesis and Electrochemical Performance of Polyacrylonitrile Carbon Nanostructure Microspheres for Supercapacitor Application. *J. Nanomater.* **2016**, *16*, 269. [CrossRef]
41. Liu, C.; Yu, Z.; Neff, D.; Zhamu, A.; Jang, B.Z. Graphene-based Supercapacitor with an Ultrahigh Energy Density. *Nano Lett.* **2010**, *10*, 4863–4868. [CrossRef]
42. Chang, H.; Wu, H. Graphene-based Nanocomposites: Preparation, Functionalization, and Energy and Environmental Applications. *Energy Environ. Sci.* **2013**, *6*, 3483–3507. [CrossRef]
43. Xia, X.; Tu, J.; Mai, Y.; Wang, X.; Gu, C.; Zhao, X. Self-supported Hydrothermal Synthesized Hollow Co_3O_4 Nanowire Arrays with High Supercapacitor Capacitance. *J. Mater. Chem.* **2011**, *21*, 9319–9325. [CrossRef]
44. Lin, J.; Wang, Y.; Zheng, X.; Liang, H.; Jia, H.; Qi, J.; Cao, J.; Tu, J.; Fei, W.; Feng, J. P-doped $NiCo_2S_4$ Nanotubes as Battery-type Electrode for High-performance Asymmetric Supercapacitor. *Dalton Trans.* **2018**, *47*, 8771–8778. [CrossRef]
45. Tang, Z.; Tang, C.; Gong, H. A High Energy Density Asymmetric Supercapacitor from Nano-architectured $Ni(OH)_2$/Carbon Nanotube Electrodes. *Adv. Funct. Mater.* **2012**, *22*, 1272–1278. [CrossRef]
46. Kirubasankar, B.; Murugadoss, V.; Lin, J.; Ding, T.; Dong, M.; Liu, H.; Zhang, J.; Li, T.; Wang, N.; Guo, Z.; et al. In Situ Grown Nickel Selenide on Graphene Nanohybrid Electrodes for High Energy Density Asymmetric Supercapacitors. *Nanoscale* **2018**, *10*, 20414–20425. [CrossRef]
47. Yu, L.; Zhang, G.; Yuan, C.; Lou, X. Hierarchical $NiCo_2O_4$@MnO_2 Core-shell Heterostructured Nanowire Arrays on Ni Foam as High-performance Supercapacitor Electrodes. *Chem. Commun.* **2013**, *49*, 137–139. [CrossRef]

48. Brisse, A.; Stevens, P.; Toussaint, G.; Crosnier, O.; Thierry, B. $Ni(OH)_2$ and NiO Based Composites: Battery Type Electrode Materials for Hybrid Supercapacitor Devices. *Materials* **2018**, *11*, 1178. [CrossRef]
49. Zhang, Y.; Ma, M.; Yang, J.; Sun, C.; Su, H.; Huang, W.; Dong, X. Shape-controlled Synthesis of $NiCo_2S_4$ and Their Charge Storage Characteristics in Supercapacitors. *Nanoscale* **2014**, *6*, 9824–9830. [CrossRef]
50. Zhang, Y.; Wang, X.; Shen, M.; Fu, X.; Huang, M.; Liu, X.; Zhang, Y.X. Uniform Growth of $NiCo_2S_4$ Nanoflakes Arrays on Nickel Foam for Binder-free High-performance Supercapacitors. *J. Mater. Sci.* **2018**, *54*, 4821–4830. [CrossRef]